

Surface Nonlinear Optics on Centrosymmetric Dirac Nodal-Line Semimetal ZrSiS

Shumeng Chi, Fei Liang, Hongxiang Chen, Wendong Tian, Han Zhang, Haohai Yu,*
 Gang Wang,* Zheshuai Lin,* Jiangping Hu, and Huaijin Zhang*

Gapless surface states (SSs) are features of topological semimetals and are extensively observed. Nowadays, the emerging question is whether the SSs possess exotic and applicable properties. Here, associated with the symmetrical selection rule for nonlinear optical materials, the surface nonlinear optics on a centrosymmetric Dirac nodal-line semimetal ZrSiS crystal is studied and it is found that the SSs bring record nonlinear susceptibilities. The unprecedented conversion efficiencies for second and third harmonic generations are 0.11‰ and 0.43‰, respectively, more than ten orders of magnitude larger than the typical surface second harmonic generation. This work discovers a new route toward studying the SSs for applications in nonlinear photonics.

Topological semimetals (TSs), featuring the nontrivial topological bulk and derived gapless surface states (SSs) with distinct electronic band structures, have drawn enormous interests and led the generation of exotic properties which may revolutionize the electronics and optoelectronics.^[1–5] The gapless SSs, coexisting or hybridizing with the bulk bands, are the most remarkable consequence of the presence of bulk nodal

points for all Weyl semimetals and some Dirac semimetals, and are identified as new topological states distinct from that in topological insulators due to the lack of a full bandgap between the bulk conduction and valence bands.^[6,7] In the view of condensed matter, the translational symmetry is broken on the surfaces of a crystal, which induces structural and dielectric abrupt discontinuity, and usually results in exceptional electronic or optoelectronic properties of the SSs. Nowadays, the SSs have been extensively studied by theoretical calculations and angle-resolved photoelectron spectroscopy (ARPES). In addition, it has been theo-

retically demonstrated that the SSs hold some extraordinary electronic properties, such as double- and quad-helical states, novel quantum oscillations in transport, as well as the strong Friedel oscillations.^[7–9] However, the experimental demonstration of the applicable properties of SSs is still rare because the SSs mainly relate to the atomic monolayer and derive from the bulk states, which means that the properties are ineluctably influenced by the bulk states and hinder the understanding in depth of the SSs for further optoelectronic applications.


In theory, the nonlinear optical (NLO) response of a matter correlates with its intrinsic properties and eigenstates of electrons,^[10,11] and today, the nonlinear optics has become the foundation of many key techniques in modern optoelectronics.^[12–14] The NLO response is dependent on the anisotropy of crystals and can distinguish the electronic response contributed from surfaces or bulk states,^[11,15,16] e.g., the second harmonics require the structural noncentrosymmetry, which can efficiently shield the contribution from the bulk states with centrosymmetric configuration. Therefore, the surface nonlinear optics could be a new noninvasive probe for surface electronic states of the TSs, especially those with bulk centrosymmetry. In the TS family, ZrSiS has centrosymmetric bulk symmetry and Dirac cones forming a diamond-shaped Fermi surface within the Brillouin zone. In addition, ZrSiS takes on large linear dispersion range of the Dirac cone partially up to 2 eV and unconventional SSs,^[17,18] which means that it provides a good platform to investigate properties of the SSs by the NLO technique and develop future applicable nonlinear devices. Herein, we studied the surface nonlinear optics of ZrSiS. Giant nonlinear susceptibilities resulting from the SSs of ZrSiS have been demonstrated for the first time, which lead to efficient second harmonic generation (SHG) and

Dr. S. Chi, Dr. W. Tian, Prof. H. Yu, Prof. H. Zhang
 State Key Laboratory of Crystal Materials and Institute
 of Crystal Materials
 Shandong University
 Jinan 250100, China
 E-mail: haohaiyu@sdu.edu.cn; huaijinzhang@sdu.edu.cn

Dr. F. Liang, Prof. Z. Lin
 Technical Institute of Physics and Chemistry
 Chinese Academy of Sciences
 Beijing 100190, China
 E-mail: zslin@mail.ipc.ac.cn

Dr. H. Chen, Prof. G. Wang, Prof. J. Hu
 Beijing National Laboratory for Condensed Matter Physics
 Institute of Physics
 Chinese Academy of Sciences
 Beijing 100190, China
 E-mail: gangwang@iphy.ac.cn

Prof. H. Zhang
 SZU-NUS Collaborative Innovation Center for Optoelectronic Science
 and Technology and Key Laboratory of Optoelectronic Devices
 and Systems of Ministry of Education and Guangdong Province College
 of Optoelectronic Engineering
 Shenzhen University
 Shenzhen 518060, China

 The ORCID identification number(s) for the author(s) of this article can be found under <https://doi.org/10.1002/adma.201904498>.

DOI: 10.1002/adma.201904498

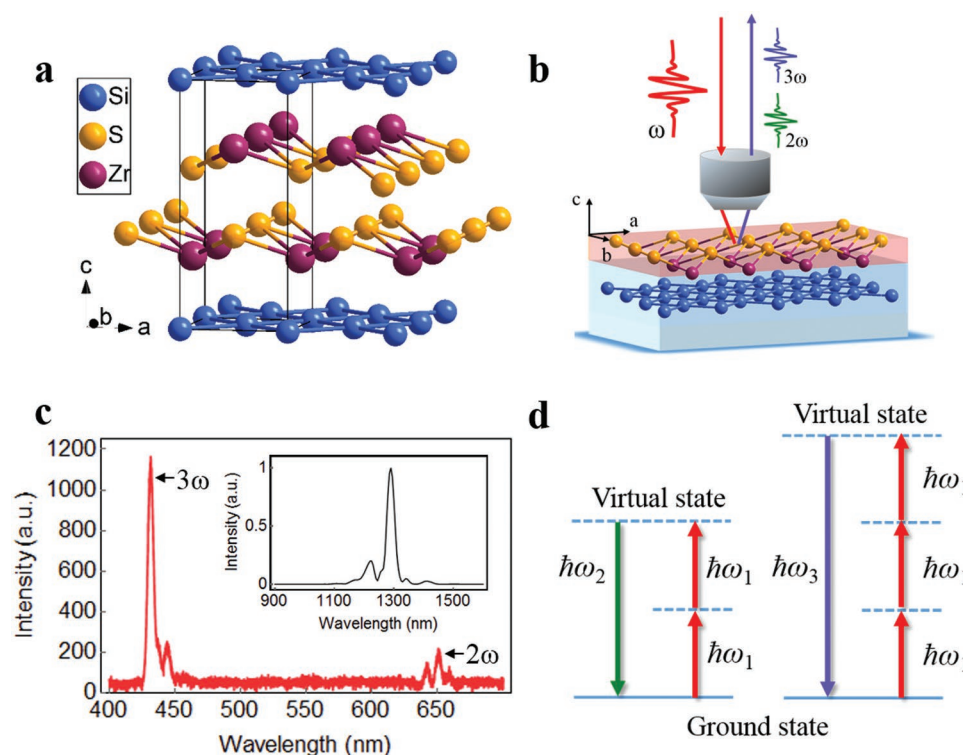


Figure 1. Schematic crystal structure and NLO measurements for ZrSiS as well as the nonlinear spectra. a) The schematic crystal structure of ZrSiS. It is a layered material composed of Zr_2S_2 and Si layers. The Zr_2S_2 layers are sandwiched between the Si square net. b) The experimental configuration for both SHG and THG measurements. The linearly polarized femtosecond pulse laser of 1300 nm was shed on the (001) surface of ZrSiS with a spot diameter about 20 μm . The objective lens (10 \times) with a numerical aperture of 0.3 was employed to focus the incident laser and simultaneously collect the SHG and THG signals, which brings about an incident angle of 17.5°. c) The spectra of SHG, THG, as well as the fundamental pump laser wave (the inset). The shoulder peaks of the output spectra are induced by the shoulder peaks of the spectra of the fundamental laser. d) Energy level diagrams describing SHG (the left panel) and THG (the right panel) processes. $\hbar\omega_1$ represents the fundamental light. $\hbar\omega_2$ and $\hbar\omega_3$ represent the SHG and THG signals, respectively. Two or three photons with frequency ω_1 are combined, and a photon with frequency $\omega_2 = 2\omega_1$ or $\omega_3 = 3\omega_1$ is simultaneously created in a single quantum-mechanical process.

third harmonic generation (THG) and remarkable conversion efficiencies for both SHG and THG.

The single-crystalline ZrSiS was grown using a chemical vapor transport method (see the Experimental Section for details). As shown in Figure 1a, ZrSiS crystallizes in a PbFCl-type crystal structure with space group $P4/nmm$, in which Si atoms form a square net and Zr atoms coordinate with four S atoms.^[19] The setup for the surface SHG and THG measurements with polarization rotation scans is schematically displayed in Figure 1b (see the Experimental Section for details). The polarized fundamental light ($\lambda = 1300$ nm) was incident on the cleaved (001) surface of the as-grown ZrSiS crystal. To eliminate the possible effect induced by different atom-terminals on NLO response of the ZrSiS surface, we have calculated SHG coefficients with both S–Zr terminal and Si-terminal models and the variation between the obtained values is small (Table S1, Supporting Information). In addition, according to the cleavage energy calculations (Figure S1, Supporting Information), S atom-terminal is the natural cleavage plane. Based on this, the S–Zr terminal model was employed for detailed calculation and analysis below. The strong peaks at the wavelengths of 650 and 433 nm were observed in the amplitude spectra (Figure 1c), which represent the SHG and THG signals converted from the fundamental light, respectively.

Notably, the intensity of THG is near 6 times as much as that of SHG, thus excluding the possibility that the THG signal is resulted from a cascaded second-order $\chi^{(2)}$ nonlinear process, namely, sum frequency generation from SHG and pump light ($\omega_3 = \omega_1 + \omega_2$). The exchange of photons between various frequencies of the field in SHG and THG processes is sketched in Figure 1d. We also performed NLO measurements with polarized fundamental lights of 1164 and 1500 nm under the same conditions, where the SHG and THG intensities show no obvious dependence on the pump wavelength in near-infrared region (Figure S2, Supporting Information).

Then, we measured the intensity of SHG and THG on ZrSiS (001) surface as a function of the incident rotation angle (Figure 2a,b). Note that ZrSiS crystallizes in a centrosymmetric tetragonal structure, which prohibits the second-order nonlinear response in the bulk. However, at the surface, the inversion symmetry is removed, which leads to a second-order dipole response defined as $P_i(2\omega) = \epsilon_0 \sum_{jk} \chi_{ijk}^{(2)}(2\omega) E_j(\omega) E_k(\omega)$ and reduces the symmetry to $4mm$ on the (001) faces, similar with the SSs as discussed in the first-principle surface electronic band calculations below.^[17,20] With an incident angle of 17.5° due to the objective lens, the polarization vector has the electric field components in three directions, including

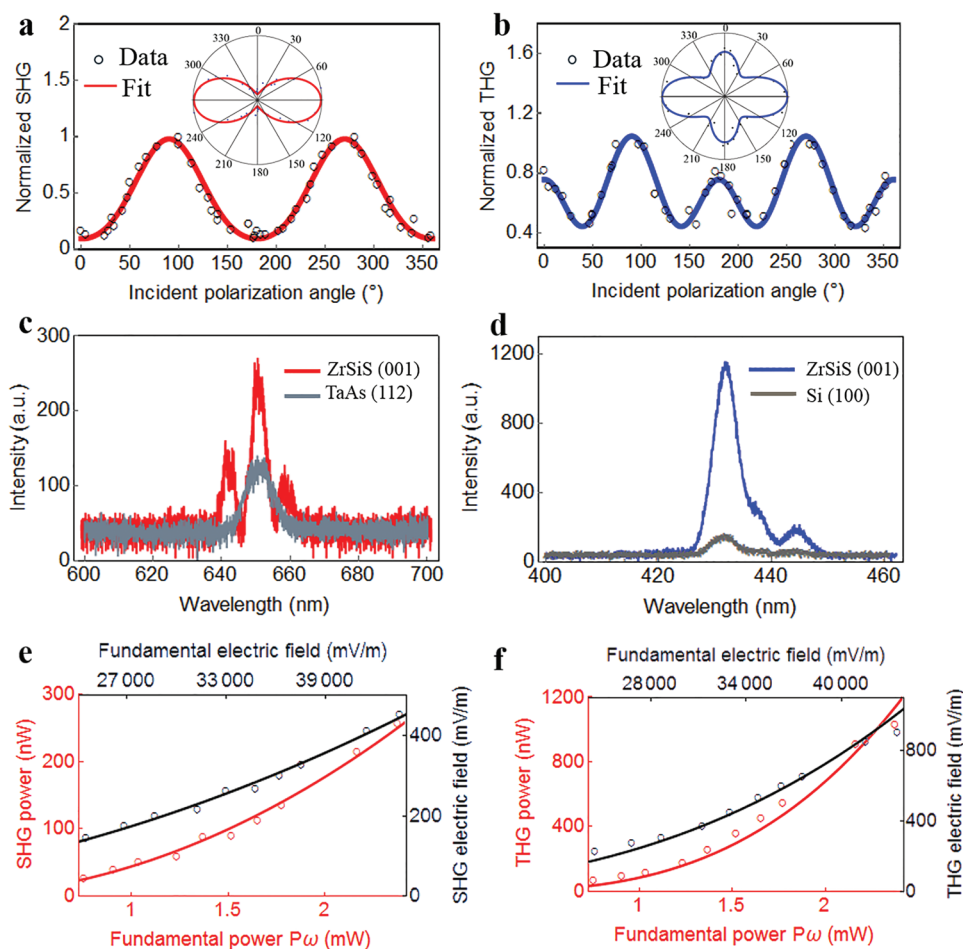


Figure 2. Experimental results for SHG and THG on (001) surface of ZrSiS. a) The SHG intensity as a function of incident polarization angle, exhibiting a quasi-two-fold symmetry (the inset). The red line is a fit. The amplitude is normalized by the peak value. b) The THG intensity as a function of incident polarization angle displaying four lobes (the inset). The blue line is a fit. The amplitude is normalized by the peak value. c) The comparison between SHG intensity of ZrSiS (001) and TaAs (112). For TaAs, the SHG signal generated by the shoulder peaks of the fundamental laser is too weak for observation. d) The THG intensity of ZrSiS (001) surface and single-crystalline silicon (100) surface. The THG peak intensity of ZrSiS exceeds that of single-crystalline silicon by about one order of magnitude. e) The SHG power as a function of the fundamental power (red circle) and the dependence of the generated harmonic field strength on the fundamental pump field strength (black circle). The lines are fits. f) The THG power as a function of the fundamental power (red circle) and the dependence of the generated harmonic field strength on the fundamental pump field strength (black circle). The lines are fits.

E_x , E_y , and E_z . Based on these facts, we derive the expression of SHG intensity

$$I \propto (0.3\chi_{15} \sin^2 \theta)^2 + (0.57\chi_{15} \sin^2 \theta)^2 + (\chi_{15} \cos^2 \theta + 0.9\chi_{15} \sin^2 \theta + 0.09\chi_{33} \sin^2 \theta)^2 \quad (1)$$

Here, θ is the rotation angle for the polarization vector with respect to the crystallographic axis a . Fitting curve derived from Equation (1) (red line in Figure 2a) shows a quasi-two-fold symmetry, which matches well with the experimental results. Using this equation, value of χ_{33}/χ_{15} falls in the range of 23–25.

To determine the value of $\chi^{(2)}$ coefficient for ZrSiS, the Weyl semimetal TaAs was selected as reference. In former report, TaAs (112) possesses a huge $\chi_{33}^{(2)}$ around 7200 (± 1100) pm V⁻¹.^[21] Following the same way in ref. [21], we collected the maximum peak intensity in the angular scan on the (112) surface of our as-grown TaAs crystal,^[22] and extracted χ_{33} of TaAs using the

method in ref. [21]. To make the comparison explicit and valid, we selected the peak intensity ($\theta = 90^\circ/270^\circ$) for ZrSiS (001) in the polar plot displayed in Figure 2a, where the intensity is proportional to $0.016|\chi_{33}|^2 \approx 0.019|\chi_{33}|^2$. Clearly, the SHG intensity of ZrSiS (001) is about 2.25 times larger than that of TaAs (112) (Figure 2c). When comparing SHG intensities from different materials, besides the nonlinear susceptibility, the index of refraction at the fundamental and the SHG frequencies should also be considered (see the Experimental Section for details). With the values for index of refraction of ZrSiS and TaAs,^[23,24] it can be deduced that $|\chi_{33}^{\text{ZrSiS}}/\chi_{33}^{\text{TaAs}}| = 0.21 - 0.23$. In addition, note that the second harmonic light here is collected in the reflection geometry, a correction considering the boundary condition for calculating $\chi_R^{(2)}$ (“R” represents the reflection geometry) is necessary. In this case, Bloembergen–Pershan formula was employed,^[21,25] with which the correction factor is calculated to be ≈ 3 (see the Experimental Section for

Table 1. The second-order nonlinear susceptibility of different materials at room temperature.

Material	Max $\chi^{(2)}$ [pm V ⁻¹]	Reference
ZrSiS	4780 (\pm 920)	This work
Monolayer MoS ₂	5000	[29]
Monolayer GaSe	2400	[30]
Monolayer h-BN	2000	[31]
GaAs	340	[32]
ZnGeP ₂	140	[32]
β -BaB ₂ O ₄	4.4	[14]

details). Accordingly, the absolute value of χ_{33} for ZrSiS is determined to be 4780 (\pm 920) pm V⁻¹, which agrees with the first-principle calculated value ($\chi_{33} \approx 4004$ pm V⁻¹) (see the Experimental Section). Considering the possible wavelength dependency of the nonlinear optical response, we carried out the SHG experiments at 800 and 1190 nm with ZrSiS (001), TaAs (112), and GaAs (111) following the same way used in ref. [21]. As shown in Figure S3 (Supporting Information), the relative peak SHG intensity among ZrSiS, TaAs, and GaAs is substantially retained. Consistent with the results at 1300 nm (Figure S4, Supporting Information), the ratio of the relative SHG intensity (≈ 6.9 times) with TaAs (112) and GaAs (111) at 800 nm is consistent with that reported (6.6 times) in ref. [21]. It is demonstrated that the second-order nonlinear optical susceptibilities of all three materials show weak wavelength dependency in the present near-infrared region (800–1300 nm). The large $\chi^{(2)}$ value of ZrSiS is higher than most of those reported in commercial bulk NLO materials as well as atomic thin NLO materials (see Table 1), and being comparable with that of well-designed nonlinear structure such as a coupled quantum well.^[26] In order to exclude the contribution from the bulk electric quadruple (EQ) response, we have investigated the incident angle dependence of the SHG intensity of ZrSiS and found that the variation of the SHG intensity is well consistent with the theoretical calculations derived from the reduced symmetry of $4mm$ at the surface (Figure S5, Supporting Information). The SHG intensity with the incident angle changing from 5° to 17.5° is improved to be 5 times, which is much smaller than that resulting from the possible EQ response (Supporting Information).^[27] It is believed that such high SHG response is different from the strong SHG induced by EQ response in centrosymmetric graphene as well as the giant SHG from the layered antiferromagnetic order in antiferromagnetic bilayer CrI₃,^[27,28] and comes from the SSs.

The THG of ZrSiS consists of four lobes with θ varying from 0 to 2π . This third-order nonlinear response can be defined in terms of an effective polarization^[14]

$$P_i(3\omega) = \epsilon_0 \sum_{jkl} \chi_{ijk}^{(3)}(3\omega) E_j(\omega) E_k(\omega) E_l(\omega) \quad (2)$$

The experimental dots of the polar pattern of THG were well fitted by the $4mm$ symmetry (blue line in Figure 2b). Single-crystalline silicon, with the third-order nonlinear susceptibility $|\chi_{33}^{(3)}| \approx 1.12 \times 10^{-13}$ m² V⁻², was selected as the reference.^[33]

Both measurements of THG on ZrSiS (001) surface and silicon (100) surface were performed under the same experimental conditions. ZrSiS exhibits a significantly enhanced peak, as compared to that of the single-crystalline silicon (Figure 2d). We found that the THG intensity ratio $I_{\text{ZrSiS}}/I_{\text{Si}}$ is about 10. Using the relation

$$\frac{|\chi_{\text{ZrSiS}}^{(3)}|}{|\chi_{\text{Si}}^{(3)}|} \approx \frac{\delta_{\text{Si}}}{\delta_{\text{ZrSiS}}} \sqrt{\frac{I_{\text{ZrSiS}}}{I_{\text{Si}}}} \quad (3)$$

and the penetration depth ratio $\delta_{\text{Si}}/\delta_{\text{ZrSiS}} \approx 21$ considering the index of refraction, through the correction considering the boundary condition in the reflection geometry as discussed (see the Experimental Section for details), we obtained the recordable third-order susceptibility $|\chi_{\text{ZrSiS}}^{(3)}| \approx 7.47 \times 10^{-12}$ m² V⁻², which exceeds many traditional NLO materials and low-dimensional materials by several orders of magnitude (see Table 2), thus demonstrating the enhanced third-order nonlinear effects observed with the reflection geometry on ZrSiS (001) surface. Since the optical penetration depth (see the Supporting Information) involves multiatomic layers, the bulk states may contribute to the THG during the electromagnetic interaction process. To quantitatively evaluate the contribution from the bulk states, we calculated the third-order nonlinear susceptibility resulting from the bulk using the typical expression in terms of fundamental physical constants^[14]

$$\chi^{(3)} \approx \frac{e^4}{\epsilon_0 m^3 \omega_0^6 d^5} \quad (4)$$

where e is the charge of the electron, m is the mass of the electron, ϵ_0 is the vacuum dielectric constant, ω_0 is the single resonance frequency, and d is the atomic dimension. Note that ω_0 and d are roughly the same for most solids. Taking $\omega_0 = 7 \times 10^{15}$ rad s⁻¹ and $d = 3$ Å,^[14] $\chi^{(3)}$ is calculated to be $\approx 3.44 \times 10^{-22}$ m² V⁻², which is ten orders of magnitude smaller than the measured value as described above. It can be deduced that the dominant contribution for THG is from the SSs, whereas the contribution from bulk states is negligible. Furthermore, we characterized the third-order nonlinear susceptibility of ZrSiS using the reflection Z-scan technique (Figure S6, Supporting Information) and $|\chi^{(3)}|$ was determined

Table 2. The third-order nonlinear susceptibility of different materials at room temperature.

Material	$\chi^{(3)}$ [m ² V ⁻²]	Reference
ZrSiS	7.47×10^{-12}	This work
Si	1.12×10^{-13}	[33]
GaAs	1.4×10^{-18}	[14]
Monolayer MoS ₂	3.6×10^{-19}	[34]
Monolayer WS ₂	2.4×10^{-19}	[34]
Ge	5.6×10^{-19}	[14,35]
ZnSe	6.2×10^{-20}	[14]
TiO ₂	2.1×10^{-20}	[14]
Diamond	2.5×10^{-21}	[14]

to be $4.85 \times 10^{-12} \text{ m}^2 \text{ V}^{-2}$ at the wavelength of 1300 nm, which has the same order of magnitude with the estimation of $7.47 \times 10^{-12} \text{ m}^2 \text{ V}^{-2}$ from comparison with single-crystalline silicon.

Figure 2e,f shows the SHG power ($P_{2\omega_0}$) and THG power ($P_{3\omega_0}$) as a function of the fundamental power (P_{ω_0}) (red circles). As fitted, the SHG and THG powers have $P_{\omega_0}^2$ and $P_{\omega_0}^3$ dependence, respectively. The 2.4 mW total power of the input pump beam after the objective yields a maximum average intensity of $I_{\omega_0} = 7.6 \times 10^6 \text{ W m}^{-2}$. The maximum conversion efficiencies $P_{2\omega_0}/P_{\omega_0}$ for SHG and $P_{3\omega_0}/P_{\omega_0}$ for THG are about 0.11% and 0.43%, respectively, corresponding to $4.5\% \text{ W}^{-1}$ for $P_{2\omega_0}/P_{\omega_0}^2$ and 74.6 W^{-2} for $P_{3\omega_0}/P_{\omega_0}^3$, which are unprecedented and about two orders of magnitude higher than the recorded surface SHG with a well-designed silica whispering-gallery microcavity under the pump of continuous wave (about 0.049% W^{-1}).^[36] and 16 orders of magnitude higher than the typical surface SHG (about $10^{-16}\% \text{ W}^{-1}$).^[37] Moreover, this value is comparable with that of commonly used transparent bulk NLO materials such as $\beta\text{-BaB}_2\text{O}_4$,^[38] and such surface nonlinear effect is more favorable for optical devices due to the integration and miniaturization. Considering the pulsed wave pump configurations here, the peak conversion efficiency was calculated. Based on the relation between the fundamental intensity and the SHG ($I_{2\omega_0} \propto I_{\omega_0}^2$) and THG ($I_{3\omega_0} \propto I_{\omega_0}^3$) intensities, the pulse widths of SHG and THG are estimated to be around 85 and 69 fs, respectively. Accordingly, the peak conversion efficiencies for SHG ($P_{2\omega_0}^{\text{peak}}/P_{\omega_0}^{\text{peak}}$) and THG ($P_{3\omega_0}^{\text{peak}}/P_{\omega_0}^{\text{peak}}$) are calculated to be about 0.15% and 0.75%, respectively.

In order to investigate the field conversion efficiency of the SHG and THG processes, we transformed the power intensity into the electric field E (black circles in Figure 2e,f). According to the relation $I \propto E^2$, the corresponding field conversion efficiencies for SHG and THG are calculated to be 1% and 2%, respectively, which are remarkable in consideration that electromagnetic interaction occurs in single or several-atomic layers. Specially, the THG field conversion efficiency is one order of magnitude higher than that of graphene in terahertz region (under the pump peak field strength of 12–61 kV cm^{-1}) and single-crystalline silicon as measured.^[39] Besides, the peak electric field conversion efficiencies are calculated to be 1.2% and 2.7% for SHG and THG under the pump peak field strength of $2.52 \times 10^3 \text{ kV cm}^{-1}$, respectively. These results clearly indicate the capacity of ZrSiS SSs for effective frequency conversion in near-infrared region, even far-infrared and terahertz region, which lay the groundwork for applications in future optoelectronics.

To understand the ultrastrong anisotropic NLO response observed on the ZrSiS (001) surface, we calculated the first-principle surface electronic band structure (Figure 3a,b), which is identical with previous reported calculations.^[17] In addition, the broken translational symmetry on the surfaces introduces an asymmetry between the two nonsymmorphic Zr sublattices. As a result, the space group of the surface slab is reduced to $P4mm$ subgroup and $4mm$ point group, which is consistent with the SHG and THG symmetry analyses above. In previous reports, the second-order nonlinearity of TSs is mainly attributed to the electron transitions between linear dispersed bands near Dirac cone.^[21,40] For ZrSiS slab, there are two

kinds of Dirac cones along Γ –M direction ($E = 0.2 \text{ eV}$) and at X point ($E = -0.5 \text{ eV}$), respectively, in which the relative energies both are smaller than that of fundamental wavelength (0.95 eV) (Figure S7, Supporting Information). However, the Dirac cone along Γ –M direction is as same as the bulk counterpart, while another Dirac cone at X point is surface-derived, which has been experimentally confirmed.^[17] In other words, the Dirac cone will strongly interact with the crossing surface bands along X– Γ and X–M directions (Figure S7, Supporting Information). At X point, the linearly dispersed bulk states are degenerate at $E_d \approx -0.5 \text{ eV}$ and gradually decrease to lower initial state energies along the X–M direction. This bulk state (BS) ranging from -1 to 1 eV is intersected by the first surface band state (SS) located at -0.2 eV , just above the degenerate point and close to the Fermi level. The second surface band state (SS') emerges at relatively lower energy ($E_{ss'} \approx -1.2 \text{ eV}$) and far away from the Fermi level. The visualized atomic orbitals reveal that the BS bands (Figure 3d) consist of Si 3p, S 3p, and Zr 4d orbitals from inside Si– and Zr–S layers, whereas the SS band is mainly composed of Zr 4d orbitals (Figure 3e) and the SS' band is mainly contributed from S 3p orbitals (Figure 3f) from surface Zr–S layers. Therefore, these two bands are exactly surface-derived bands, which form the nontrivial SSs.^[17,18] Moreover, SS does not originate from band inversion because it does not start at a Dirac point.

In previous report,^[23] the first-order optical properties and flat optical conductivity of ZrSiS have been assigned to the transitions between quasi-2D Dirac bands near the Fermi level. Similarly, the giant optical nonlinearity can also be attributed to the virtual electronic excitations near Fermi level in ZrSiS slab. The valence electrons reconstruct at ZrSiS surface owing to the broken symmetry, thereby yielding a floating 2D band (SS) close to the Fermi level. Band resolved SHG analysis for $\chi_{33}^{(2)}$ (Figure 3c) demonstrated that there are several peaks contributing for strengthened SHG coefficients ranging from -0.2 to 0.5 eV , which basically correspond to SS near Fermi level. This phenomenon is consistent with our previous conclusions in traditional semiconducting NLO crystals.^[41] Besides SS, there is also tiny contribution from SS' below -1 eV . However, owing to that it is fully occupied and far away from Fermi level, the contribution from SS' is nearly negligible. Thus, the introduction of floating SS band improves the intensity of electron states and boosts the enhanced SHG response on ZrSiS surface. Therefore, our studies demonstrated that the NLO effect is a credible tool for the detection of the surface electronic states induced by the translational symmetry breaking, which enables the mapping of the symmetry properties for SSs.

Finally, it should be noted that the interaction and counteraction between photons and electrons are interrelated. In this work, we demonstrated that the surface electron states of ZrSiS hold the capacity to convert the photon frequency with high efficiency. On the other hand, the surface electrons of ZrSiS, as well as other topological materials, can also be affected by the applied strong laser field. We believe this phenomenon will be detected in future transient spectroscopy experiments combining ARPES and laser irradiation. Nonlinearity under strong laser field is expected to provide a powerful tool to modulate the electron states of condensed matter, as well as the corresponding magnetic, valley, and transport properties.

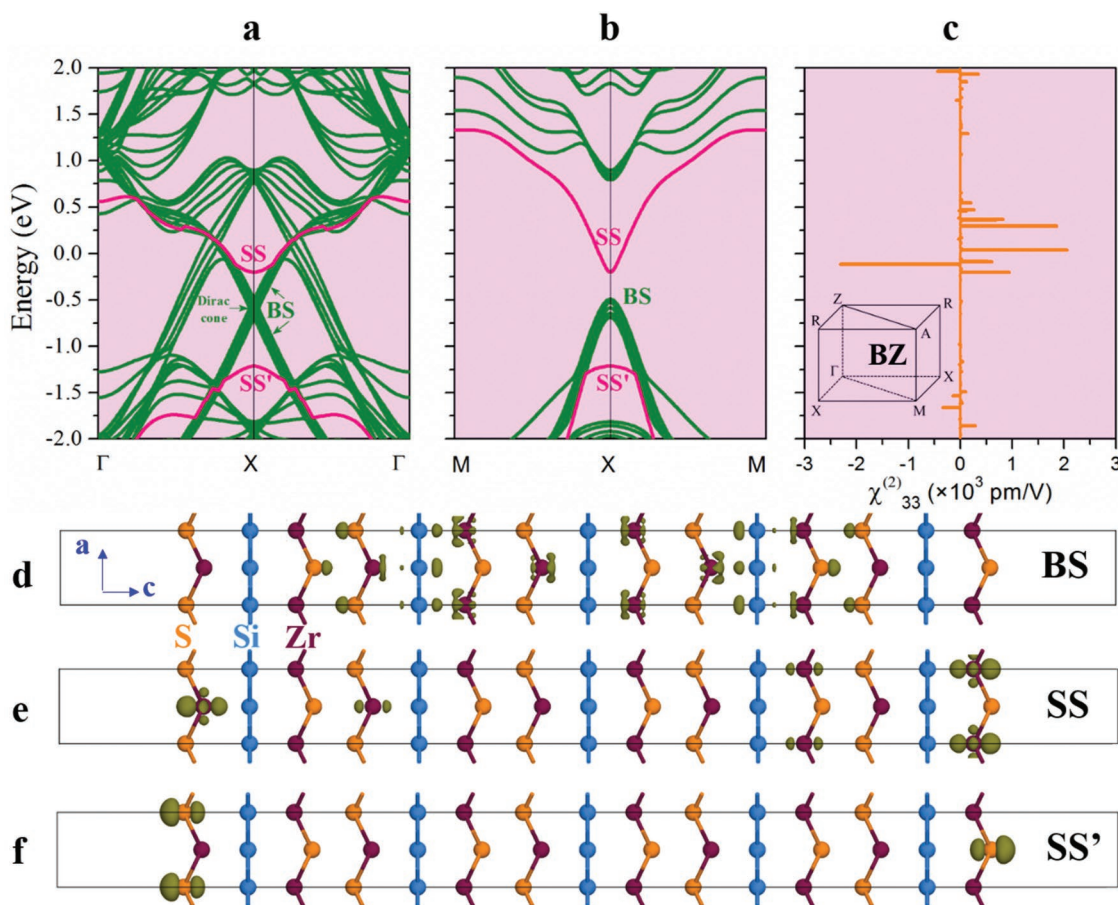


Figure 3. First-principle calculations of surface electronic band structure. a,b) The calculated slab band structures along the X- Γ (a) and X-M (b) directions, respectively. BS represents the bulk bands and SS, SS' represent the surface bands. c) The band resolved $\chi_{33}^{(2)}$ of ZrSiS slab. The dominated peaks for $\chi_{33}^{(2)}$ are related to SS near Fermi level. The inset is the Brillouin zone (BZ) of a primitive tetragonal lattice for ZrSiS. d-f) The visualized atomic orbitals of BS (-2.93 to -0.52 eV), SS (from -0.10 to 1.38 eV), and SS' (from -2.92 to -1.13 eV). The BS bands (d) consist of Si 3p, S 3p, and Zr 4d orbitals. SS band (e) is mainly composed of Zr 4d orbitals, and the SS' band (f) is mainly contributed from S 3p orbitals.

In summary, this work studied the nonlinear surface optics and experimentally revealed the strong anisotropic nonlinear response on the surface of Dirac nodal-line semimetal ZrSiS. Based on the symmetrical selection rule for NLO materials, the SSs with lowered symmetry is responsible for the efficient SHG since the bulk state of ZrSiS is centrosymmetric, as well as giant THG with high conversion efficiency. More importantly, the structural and symmetry informations of the SSs are detected by the optical spectra involved in nonlinear response. This work not only discovers the giant nonlinear response of the topological SSs, but also creates a novel roadmap toward exploration and application of surface nonlinear optics and photonics.

Experimental Section

Crystal Growth and Characterization: Single crystals of ZrSiS were grown using a chemical vapor transport method. First, Zr (Aladdin, 99.95%), Si (Alfa Aesar, 99.9%), and S (Alfa Aesar 99.99%) powders with a mole ratio Zr:Si:S = 1:1:1 and a small amount of I_2 (3 mg cm⁻³) were loaded into an evacuated quartz tube. Then, the sealed quartz ampoule was heated in a two-zone tube furnace for 7 days.

The ingredients were transported from the hot zone (1150 °C) to the cool zone (1070 °C) and ZrSiS single crystals were grown. The obtained ZrSiS single crystals had shiny surfaces. The cleaved (001) surface of the as-grown ZrSiS single crystal was used for NLO measurements. X-ray diffraction was performed to verify the orientation of the measured surface, as shown in Figure S8 (Supporting Information), indicating that the surface was along the (001) plane and demonstrating the high quality in crystallinity. In addition, the energy-dispersive X-ray spectroscopy measurement was applied to characterize the elemental composition on the cleaved surface (Figure S9, Supporting Information).

Optical Setup for NLO Response Measurements: The setup for the surface SHG and THG measurements with polarization rotation scans is schematically displayed in Figure 1b. The pulsed fundamental lasers were provided by an optical parametric amplification with a pulse having width of 120 fs and repetition rate of 1 KHz, and were normally incident on the farthest position (5.6 mm) from the optical axis of the objective (numerical aperture = 0.3), i.e., the closest to the diametral line of the objective, inducing an incident angle of 17.5° and a spot diameter about 20 μ m on the (001) surface of ZrSiS. A half wave plate was rotated to modulate the polarization vector of the fundamental laser and a Glan-laser prism with a polarization degree of 1/100 000 was put after the half wave plate to ensure the polarization degree and verify the polarization direction. The reflected SHG and THG signals collected by

the objective lens were coupled to an optical fiber and finally reached the spectrometer, which could directly analyze the wavelength and intensity of the signals. The powers of SHG and THG were measured by a power meter with high accuracy. To distinguish the SHG and THG signals, the narrow-band filters were employed.

First-Principle Calculation Methods: All density functional theory calculations were performed by CASTEP code.^[42] The lattice parameters and the atomic positions in the unit cell of ZrSiS and TaAs were fully optimized. The convergence threshold for self-consistent field tolerance was set as 1.0×10^{-9} eV atom⁻¹. The semiempirical OBS ($\lambda = 0.00075$ and $n = 8$) dispersion correction methods (methods developed by Ortman, Bechstedt, and Schmidt) were used to treat the van der Waals interactions between the adjacent layers.^[43] The optimized lattice parameters of ZrSiS ($a = 3.526$ Å, $c = 7.962$ Å) and TaAs ($a = 3.375$ Å, $c = 11.40$ Å) were consistent with the experimental values ($a = 3.544$ Å, and $c = 8.055$ Å;^[19] $a = 3.436$ Å, and $c = 11.64$ Å^[44]), respectively. A five unit cell thick ZrSiS (001) slab was constructed similar to that in the work of Schoop et al.^[17] A kinetic energy cutoff of 900 eV was chosen with Monkhorst–Pack k -point meshes ($7 \times 7 \times 2$ for bulk ZrSiS; $30 \times 30 \times 3$ for bulk ZrSiS slab; $7 \times 7 \times 2$ for bulk TaAs) spanning less than 0.04 Å⁻³ in the Brillouin zone.^[45] The Brillouin zone path in the reciprocal space was as same as that of TaAs by Weng et al.^[5] and ZrSiS by Schoop et al.^[17] Based on the calculated electronic structure, the second-order susceptibility $\chi^{(2)}$ was calculated using an expression originally proposed by Rashkeev et al.^[46] and developed by Lin et al.^[47]

Calculation Procedure of χ_{33} and $\chi^{(3)}$ for ZrSiS Surface: When the nonlinear interaction length could be neglected, such as on the surface, the relation between SHG intensity I and the intensity of polarization P was defined as^[14]

$$I = MP^2 = \frac{2\omega^2}{c^3 n^2(\omega) n(2\omega) \epsilon_0} P^2 \quad (5)$$

where n is the complex index of refraction, M is the factor between I and P^2 . Taking the values of index of refraction for ZrSiS and TaAs,^[23,24] the ratio for M between ZrSiS and TaAs was calculated to be ≈ 33.3 .

According to the Bloembergen–Pershan formula^[25]

$$\chi_R^{(2)} \equiv -\frac{E_R(2\omega)}{\epsilon_0 E(\omega)^2} \quad (6)$$

$$E_R(2\omega) = -4\pi P \frac{1}{\sqrt{\epsilon'(\omega) + i\epsilon''(\omega)} + 1} \times \frac{1}{\sqrt{\epsilon'(\omega) + i\epsilon''(\omega)} + \frac{1}{2}(\epsilon'(\omega) + i\epsilon''(\omega)) + \frac{1}{2}\sqrt{\epsilon'(\omega) + i\epsilon''(\omega)}} \quad (7)$$

where ϵ' and ϵ'' are the real and imaginary parts of the complex dielectric constant. The correction factor was estimated to be ≈ 3 using the complex dielectric constant reported in ref. [23].

Just as the SHG, the THG was also determined in the reflection geometry. With the relation^[48]

$$E_R(3\omega) = F^R \left[\chi^{(3)} \right] E^3(\omega) \quad (8)$$

$$F^R = \left(\frac{1024\pi^2}{\left[1 + \sqrt{\epsilon'(\omega) + i\epsilon''(\omega)} \right]^6 \left[1 + \sqrt{\epsilon'(3\omega) + i\epsilon''(3\omega)} \right]^2 \left[\sqrt{\epsilon'(\omega) + i\epsilon''(\omega)} + \sqrt{\epsilon'(3\omega) + i\epsilon''(3\omega)} \right]^2} \right)^{\frac{1}{2}} \quad (9)$$

and the boundary condition derived by Bloembergen and Pershan,^[25] the correction factor was estimated to be fairly small (≈ 1.03).

Supporting Information

Supporting Information is available from the Wiley Online Library or from the author.

Acknowledgements

S.C. and F.L. contributed equally to this work. This work was financially supported by the National Natural Science Foundation of China (Grant Nos. 51772173, 51832010, 51702330, 51802321, and 51632004), the National Key Research and Development Program of China (Grant Nos. 2018YFE0202600, 2017YFA0302902, 2016YFB0701002, and 2016YFB1102301), and the Provincial Key Research and Development Program of Shandong (Grant No. 2017CXGC0414). Z.L. acknowledges support from the Youth Innovation Promotion Association, Chinese Academy of Sciences (CAS).

Conflict of Interest

The authors declare no conflict of interest.

Keywords

density functional theory calculations, nonlinear optics, surface states, symmetry breaking, ZrSiS

Received: July 13, 2019

Revised: October 15, 2019

Published online: November 21, 2019

- [1] Z. Wang, H. Weng, Q. Wu, X. Dai, Z. Fang, *Phys. Rev. B* **2013**, *88*, 125427.
- [2] C. Shekhar, A. K. Nayak, Y. Sun, M. Schmidt, M. Nicklas, I. Leermakers, U. Zeitler, Y. Skourski, J. Wosnitza, Z. Liu, *Nat. Phys.* **2015**, *11*, 645.
- [3] T. Liang, Q. Gibson, M. N. Ali, M. Liu, R. Cava, N. Ong, *Nat. Mater.* **2015**, *14*, 280.
- [4] Z. Liu, B. Zhou, Y. Zhang, Z. Wang, H. Weng, D. Prabhakaran, S.-K. Mo, Z. Shen, Z. Fang, X. Dai, *Science* **2014**, *343*, 864.
- [5] H. Weng, C. Fang, Z. Fang, B. A. Bernevig, X. Dai, *Phys. Rev. X* **2015**, *5*, 011029.
- [6] S.-Y. Xu, C. Liu, S. K. Kushwaha, R. Sankar, J. W. Krizan, I. Belopolski, M. Neupane, G. Bian, N. Alidoust, T.-R. Chang, H.-T. Jeng, C.-Y. Huang, W.-F. Tsai, H. Lin, P. P. Shibayev, F.-C. Chou, R. J. Cava, M. Z. Hasan, *Science* **2015**, *347*, 294.
- [7] X. Wan, A. M. Turner, A. Vishwanath, S. Y. Savrasov, *Phys. Rev. B* **2011**, *83*, 205101.
- [8] C. Fang, L. Lu, J. Liu, L. Fu, *Nat. Phys.* **2016**, *12*, 936.
- [9] P. Hosur, *Phys. Rev. B* **2012**, *86*, 195102.
- [10] K. L. Seyler, J. R. Schaibley, P. Gong, P. Rivera, A. M. Jones, S. Wu, J. Yan, D. G. Mandrus, W. Yao, X. Xu, *Nat. Nanotechnol.* **2015**, *10*, 407.
- [11] X. Yin, Z. Ye, D. A. Chenet, Y. Ye, K. O'Brien, J. C. Hone, X. Zhang, *Science* **2014**, *344*, 488.
- [12] D. Strickland, G. Mourou, *Opt. Commun.* **1985**, *55*, 447.
- [13] J.-W. Pan, S. Gasparoni, M. Aspelmeyer, T. Jennewein, A. Zeilinger, *Nature* **2003**, *421*, 721.
- [14] R. W. Boyd, *Nonlinear Optics*, Elsevier, Singapore **2003**, pp. 33–212.
- [15] R. M. Corn, D. A. Higgins, *Chem. Rev.* **1994**, *94*, 107.
- [16] T. Heinz, H. Tom, Y. R. Shen, *Phys. Rev. A* **1983**, *28*, 1883.

- [17] L. M. Schoop, M. N. Ali, C. Straßer, A. Topp, A. Varykhalov, D. Marchenko, V. Duppel, S. S. P. Parkin, B. V. Lotsch, C. R. Ast, *Nat. Commun.* **2016**, 7, 11696.
- [18] M. Neupane, I. Belopolski, M. M. Hosen, D. S. Sanchez, R. Sankar, M. Szlawska, S.-Y. Xu, K. Dimitri, N. Dhakal, P. Maldonado, *Phys. Rev. B* **2016**, 93, 201104.
- [19] A. Klein Haneveld, F. Jellinek, *Recl. Trav. Chim. Pays-Bas* **1964**, 83, 776.
- [20] X. Wang, X. Pan, M. Gao, J. Yu, J. Jiang, J. Zhang, H. Zuo, M. Zhang, Z. Wei, W. Niu, Z. Xia, X. Wan, Y. Chen, F. Song, Y. Xu, B. Wang, G. Wang, R. Zhang, *Adv. Electron. Mater.* **2016**, 2, 1600228.
- [21] L. Wu, S. Patankar, T. Morimoto, N. L. Nair, E. Thewalt, A. Little, J. G. Analytis, J. E. Moore, J. Orenstein, *Nat. Phys.* **2017**, 13, 350.
- [22] Z. Li, H. Chen, S. Jin, D. Gan, W. Wang, L. Guo, X. Chen, *Cryst. Growth Des.* **2016**, 16, 1172.
- [23] M. Schilling, L. Schoop, B. Lotsch, M. Dressel, A. Pronin, *Phys. Rev. Lett.* **2017**, 119, 187401.
- [24] J. Buckeridge, D. Jevdokimovs, C. Catlow, A. Sokol, *Phys. Rev. B* **2016**, 93, 125205.
- [25] N. Bloembergen, P. Pershan, *Phys. Rev.* **1962**, 128, 606.
- [26] C. Sirtori, F. Capasso, J. Faist, L. Pfeiffer, K. West, *Appl. Phys. Lett.* **1994**, 65, 445.
- [27] Y. Zhang, D. Huang, Y. Shan, T. Jiang, Z. Zhang, K. Liu, L. Shi, J. Cheng, J. E. Sipe, W.-T. Liu, S. Wu, *Phys. Rev. Lett.* **2019**, 122, 047401.
- [28] Z. Sun, Y. Yi, T. Song, G. Clark, B. Huang, Y. Shan, S. Wu, D. Huang, C. Gao, Z. Chen, M. McGuire, T. Cao, D. Xiao, W.-T. Liu, W. Yao, X. Xu, S. Wu, *Nature* **2019**, 572, 497.
- [29] N. Kumar, S. Najmaei, Q. Cui, F. Ceballos, P. M. Ajayan, J. Lou, H. Zhao, *Phys. Rev. B* **2013**, 87, 161403.
- [30] X. Zhou, J. Cheng, Y. Zhou, T. Cao, H. Hong, Z. Liao, S. Wu, H. Peng, K. Liu, D. Yu, *J. Am. Chem. Soc.* **2015**, 137, 7994.
- [31] Y. Li, Y. Rao, K. F. Mak, Y. You, S. Wang, C. R. Dean, T. F. Heinz, *Nano Lett.* **2013**, 13, 3329.
- [32] V. G. Dmitriev, G. G. Gurzadyan, D. N. Nikogosyan, *Handbook of Nonlinear Optical Crystals*, Springer, Germany **2013**.
- [33] Y. Chen, G. Carter, *Appl. Phys. Lett.* **1982**, 41, 307.
- [34] A. Autere, H. Jussila, A. Marini, J. Saavedra, Y. Dai, A. Säynätjoki, L. Karvonen, H. Yang, B. Amirsolaimani, R. A. Norwood, *Phys. Rev. B* **2018**, 98, 115426.
- [35] N. Bloembergen, W. K. Burns, M. Matsuoka, *Opt. Commun.* **1969**, 1, 195.
- [36] X. Zhang, Q.-T. Cao, Z. Wang, Y.-x. Liu, C.-W. Qiu, L. Yang, Q. Gong, Y.-F. Xiao, *Nat. Photonics* **2019**, 13, 21.
- [37] C. Tian, Y. Shen, *Surf. Sci. Rep.* **2014**, 69, 105.
- [38] D. Nikogosyan, *Appl. Phys. A: Solids Surf.* **1991**, 52, 359.
- [39] H. A. Hafez, S. Kovalev, J.-C. Deinert, Z. Mics, B. Green, N. Awari, M. Chen, S. Germanskiy, U. Lehnert, J. Teichert, *Nature* **2018**, 561, 507.
- [40] T. Morimoto, N. Nagaosa, *Sci. Adv.* **2016**, 2, e1501524.
- [41] M. Luo, F. Liang, Y. Song, D. Zhao, N. Ye, Z. Lin, *J. Am. Chem. Soc.* **2018**, 140, 6814.
- [42] S. J. Clark, M. D. Segall, C. J. Pickard, P. J. Hasnip, M. I. Probert, K. Refson, M. C. Payne, *Z. Kristallogr. - Cryst. Mater.* **2005**, 220, 567.
- [43] F. Ortmann, F. Bechstedt, W. Schmidt, *Phys. Rev. B* **2006**, 73, 205101.
- [44] H. Boller, E. Parthé, *Acta Crystallogr.* **1963**, 16, 1095.
- [45] H. J. Monkhorst, J. D. Pack, *Phys. Rev. B* **1976**, 13, 5188.
- [46] S. N. Rashkeev, W. R. Lambrecht, B. Segall, *Phys. Rev. B* **1998**, 57, 3905.
- [47] J. Lin, M.-H. Lee, Z.-P. Liu, C. Chen, C. J. Pickard, *Phys. Rev. B* **1999**, 60, 13380.
- [48] W. Burns, N. Bloembergen, *Phys. Rev. B* **1971**, 4, 3437.